

Nanoscale

Accepted Manuscript

This article can be cited before page numbers have been issued, to do this please use: C. J. Neal, A. S. Pugazhendhi, E. Shiffer, C. R. Fox, M. H. M. Kalyar, E. Kolanthai, K. Stan-Glowinska, D. Brown, K. M. Ta, J. Wojewoda-Budka, N. Sobczak, M. Molinari, G. Parks, M. Coathup and S. Seal, *Nanoscale*, 2026, DOI: 10.1039/D5NR05105C.



This is an Accepted Manuscript, which has been through the Royal Society of Chemistry peer review process and has been accepted for publication.

Accepted Manuscripts are published online shortly after acceptance, before technical editing, formatting and proof reading. Using this free service, authors can make their results available to the community, in citable form, before we publish the edited article. We will replace this Accepted Manuscript with the edited and formatted Advance Article as soon as it is available.

You can find more information about Accepted Manuscripts in the [Information for Authors](#).

Please note that technical editing may introduce minor changes to the text and/or graphics, which may alter content. The journal's standard [Terms & Conditions](#) and the [Ethical guidelines](#) still apply. In no event shall the Royal Society of Chemistry be held responsible for any errors or omissions in this Accepted Manuscript or any consequences arising from the use of any information it contains.

ARTICLE

Persistent, Broad-Spectrum Antimicrobial Activity by Multi-Metal Surface Phase Modified Ceria Nanozymes

Craig J. Neal¹, Abinaya Sindu Pugazhendhi², Elisabeth M. Shiffer³, Candace R. Fox³, Muhammad Hassan Mehmood Kalyar³, Elayaraja Kolanthai¹, Katarzyna Stan-Glowinska⁴, Daniel Brown⁵, Khao Minh Ta⁵, Joanna Wojewoda-Budka⁴, Natalia Sobczak⁴, Marco Molinari⁵, Griffith D. Parks³, Melanie J. Coathup², Sudipta Seal^{1,3}

Received 00th January 20xx,
Accepted 00th January 20xx

DOI: 10.1039/x0xx00000x

With the growing threat of emergent microbes, such as novel viruses and drug-resistant bacteria, more robust and broad-spectrum antimicrobial technologies are of critical importance. Nanomaterials have the potential to deliver a broad-spectrum antimicrobial effect while maintaining resistance to degradation in various application environments. In the presented study, a multi-metal oxide nanoparticle formulation with substantial antimicrobial activity was developed: outperforming a previous bimetallic composition. The formulation was produced through a variation of an established method wherein the multi-metal oxide is formed through precursor ageing in a peroxide solution environment (room temperature, 8 week ageing period). Silver/zinc-modified cerium oxide nanoparticles exhibited substantial antiviral (0.05 mg/mL reduced virus titer to beyond detectable ranges for RV14 rhinovirus, ~3-log reduction for vesicular stomatitis virus on treatment with 0.15 mg/mL in TCID₅₀) and antibacterial (MIC values of ~4, 6, and 6 µg/mL, respectively, for *P. aeruginosa*; *S. aureus*, and methicillin-resistant *S. aureus* (MRSA)) activities. Of further interest, this nano-formulation evidenced persistent antibacterial activity towards bacterial (*P. aeruginosa*, *S. aureus*) and viral (RV14 rhinovirus; Vesicular stomatitis virus, VSV) lab strains resistant to previously developed silver-modified cerium oxide nanoparticles. Nanomaterial character and potential antimicrobial mechanisms were also investigated, with enzyme-mimetic *nanozyme* generation of reactive oxygen species suggested by density functional theory calculations.

1. Introduction

Human infection by pathogenic microbes continues to be a prominent societal issue, with hospital-acquired infections, emergence of novel viral variants, and growth of drug-resistant bacterial strains heightening the general health threat⁽⁵⁾. Central to these issues is the ability of microbes to circumvent or surmount traditional antimicrobial interventions and the inherent difficulties in optimally deploying these methods in certain formats, such as high-touch surfaces in public spaces⁽³⁻⁵⁾.

The use of nanomaterials has been seen as an attractive approach to address these challenges, given their versatility as functional materials and their greater physicochemical stability over organic antibiotics and antivirals and other conventional antimicrobial materials ^{(6) (7) (8) (9) (10) (11)}. This stability for

inorganic nanomaterials translates to robust activity across temperature ranges and a continuous, sustained activity over technologically relevant time periods (*i.e.*, mechanisms which do not rely on material consumption or irreversible alteration; potential for prolonged systemic dispersion, potential for catalytic reaction mechanisms, *etc.*) ^{(12) (13) (14)}. Among these nanomaterials, metal oxide-based compositions are particularly attractive for biomedical applications because of their stability towards oxidation by the biological environment ^{(15) (16) (17) (18, 19)}.

Cerium oxide is a metal oxide with substantial utility across numerous industrial sectors, due largely to its surface redox chemistry facilitated by the interconversion of cerium sites between Ce³⁺ and Ce⁴⁺ accompanied by the formation or healing of oxygen vacancies. In biomedical studies, surface redox reactions by cerium oxide nanoparticles (CNPs) have been identified as mimetic of reactions produced by enzymes ^{(20) (21) (22)}. The class of materials which produce these catalytic reactions are known as *nanozymes*. These materials, including CNPs, demonstrate the above-mentioned stability and thereby show a strong advantage over biological enzymes. Indeed, multiple studies have been published highlighting the utility of pure CNPs, produced by assorted wet chemical synthetic approaches, in antimicrobial applications. Among these studies, smaller particle sizes and surface densities of Ce³⁺ states have been reported as key metrics for the observed activities ⁽¹⁴⁾. Understanding of essential nanomaterial

¹ Materials Science & Engineering Department, Advanced Materials Processing and Analysis Center (AMPAC), University of Central Florida, Orlando, FL, 32816, United States

² Biionix Faculty Cluster, College of Medicine, University of Central Florida, Orlando, Florida 32827, United States

³ Burnett School of Biomedical Sciences, College of Medicine, University of Central Florida, Orlando, Florida 32827, United States

⁴ Institute of Metallurgy and Materials Science, Polish Academy of Sciences, Krakow, 30-418, Poland

⁵ Department of Physical and Life Sciences, School of Applied Sciences, University of Huddersfield, Huddersfield, HD1 3DH, UK

Supplementary Information available: Figures S1, S2 and S3, Tables S1 and S2



structure-property relations has progressed such that production of designer nanomaterials for specific applications, e.g. as high-efficacy antimicrobial technologies, is becoming more feasible and practical (23) (24) (7) (25) (26).

In many studies, surface redox processes have been coupled with other chemical processes to facilitate catalytic reactions of industrial relevance (i.e., soot reduction by silver-modified cerium oxide surfaces) (27) (28). In these reactions, such as the case of nanoscale silver-cerium oxide, interface formation between phases allows for coupling of charge and/or mass transfer processes to produce complex reactions (29) (30). In biomedical applications, similarly structured nanomaterials have been produced to accomplish a larger set of relevant reactions, including as antimicrobial compositions. Antimicrobial activity for these materials is often attributed to an increase in reactive oxygen species (ROS) generation and/or the release of metal ions. Therefore, noble and transition metal compositions have seen substantial investigation; e.g., Ag/Cu, Au/Pt, Cu/Zn, CuO/Ag, Ag/ZnO (11) (31) (32). (33) (34).

The presented work is built from several of our earlier investigations which demonstrated the use of leeching-stable AgCNP formulations for antiviral and antibacterial applications (1, 35, 36). In these studies, material properties including particle size, morphology, and chemical state distributions (i.e., cerium redox states, Ce³⁺/Ce⁴⁺; Ag⁰, Ag⁺), were defined for different silver-cerium oxide nanoparticle formulations and related to virus (rhinovirus, RV14; parainfluenza virus, PIV5; coronaviruses, OC43 and SARS-CoV2) or bacteria (*Pseudomonas aeruginosa*; *Staphylococcus aureus*; methicillin-resistant *S. aureus* (MRSA)) interactions. In the current work, we consider the efficacy of a nanomaterial formulation with greater compositional complexity, cerium oxide nanoparticles surface modified with silver- and zinc- rich phases, as a multi-metal material for antimicrobial applications. In these studies, we hypothesize that inclusion of both transition metals would alter the material's surface redox reaction profile through introduction of additional metal (oxide) domains and/or alteration in silver charge transfer by alloying or complex formation. An initial material characterization and analysis was performed using, primarily, high-resolution transmission electron microscopy, energy-dispersive spectroscopy, and x-ray photoelectron spectroscopy. To facilitate comparison against previously reported silver-modified cerium oxide nanoparticles, studies were performed to assess the material's antiviral/microbials efficacy towards the viruses vesicular stomatitis virus (VSV) and rhinovirus (RV14) and to the bacterial species *P. aeruginosa*, *S. aureus*, and methicillin-resistant *S. aureus* (MRSA). Results and analyses from these and related density functional theory-based studies were then used to identify possible mechanisms of observed substantial antimicrobial activities for the silver/zinc-modified cerium oxide nanoparticle formulation.

2. Materials and Methods

2.1 Materials Synthesis and Characterization

2.1.1 Synthesis A nanoparticle formulation was produced incorporating silver and zinc with cerium oxide nanoparticle through a one-pot synthesis, similar to a previously reported method(36). A quiescent aqueous solution of 1.0 mM zinc nitrate (99.5% purity), 1.0 mM silver nitrate (99.9% purity), and 5.0 mM cerium nitrate hexahydrate (99.999% purity) (final molar concentrations) in a borosilicate storage bottle was treated with 2 mL of 3% hydrogen peroxide solution for a final solution volume of 50 mL. The solution was then homogenized *via* vortex mixer continuously for 2 minutes, the bottle's cap was loosened to allow release of evolved gases, and the solution was stored, without perturbation, in dark conditions for up to 8 weeks prior to characterization. All chemical manipulations were performed at standard temperature and pressure. All chemicals were purchased from *Sigma Aldrich* and were used without further modification.

2.1.2 X-ray Photoelectron Spectroscopy Samples were prepared by drying from solution onto clean gold foil substrates inside of a chemical fume-hood at room temperature. Measurements were performed using an ESCALAB-250 Xi spectrometer with a monochromatic Al-K α radiation source under a vacuum < 1x10⁻⁹ mbar, operating power of 300 W (150 kV, 20 mA), pass energy of 20 eV, step size of 0.1 eV, and a spot size of 650 μ m. All spectra were referenced to the C-C/C-H binding energy, within the C1s region, assigned a value of 284.6 eV. Peak assignment was performed based on reported values from relevant published literature.

2.1.3 High-resolution Transmission Electron Microscopy Samples for the transmission electron microscopy (TEM) studies were prepared according to the following procedure: a droplet of the aqueous suspension containing nanoparticles was poured onto the copper grid covered with a thin carbon layer and dried on air. Detailed analysis of nanoparticles was performed including bright field imaging (BF), selected area diffraction patterns (SADP), high resolution imaging in TEM (HRTEM) and the Scanning Transmission Electron Microscopy High-Angle Annular Dark Field mode (STEM) including mapping of elemental distribution in the selected areas using Themis G2 200 Probe Cs-corrected transmission electron microscope operating at 200 kV and equipped with X-FEG, HAADF-STEM and Super-X EDX System.

2.1.4 Computational Methodology Spin-polarized density functional calculations were run using the VASP code (37-39). The frozen-core projector-augmented wave (PAW) method was utilized with a plane-wave basis set with a cutoff of 500 eV (39, 40). 3D boundary conditions were implemented. The cut-off energy and k-point mesh have been checked for convergence as in our previous calculations. The exchange correlation functional was the Perdew-Burke-Ernzerhof (PBE) GGA (1, 2, 41, 42). An effective U = 5 eV was used on the Ce f orbitals using the Dudarev method (43) to enable localization of Ce³⁺ states as in our previous studies (44-46). METADISE code was used to



generate all models (47). The conventional 12-atom bulk CeO₂ unit cell was simulated with the electronic and ionic convergence criteria of 1×10⁻⁵ eV and 1×10⁻³ eV Å⁻¹, respectively, and the Brillouin zone sampled using a Γ -centered 5 × 5 × 5 k-point mesh. The simulated lattice constant (5.498 Å, space group 225) is overestimated as in previous computational studies due to the usage of the PBE+U methodology (48-54). The CeO₂ surface models were simulated using the slab method, where the top and the bottom of the slab are allowed to relax. The {100}, {110} and {111} surfaces are $\sqrt{2} \times \sqrt{2}$, $\sqrt{2} \times 2$ and $\sqrt{2} \times \sqrt{2}$ expansions with 7 (28 CeO₂ units), 7 (28 CeO₂ units) and 5 (20 CeO₂ units) surface layers, respectively. To remove the dipole of the {100} slab, half of the surface oxygen atoms were moved from one side to the other of the slab. A vacuum gap of 15 Å perpendicular to the surface was introduced to minimize the interaction between images. The surfaces were simulated using the electronic and ionic convergence criteria of 1×10⁻⁵ eV and 1×10⁻² eV Å⁻¹, respectively, with the Brillouin zone sampled using a Γ -centered 2 × 2 × 1 k-point mesh, with the third vector perpendicular to the surface plane. Oxygen vacancies (on the surface and subsurface layer), Zn dopant atoms and adsorbates were introduced symmetrically on both sides. To reduce the exploration of the configurational space for the adsorption of species, only models based on previous studies were used (1, 2). The adsorbate species (*i.e.* isolated H₂O₂ and O₂ molecules, and Ag₃ cluster) were geometry optimized in a cubic cell of side 10 Å at the Γ point with the electronic and ionic convergence criteria of 1×10⁻⁵ eV and 1×10⁻² eV Å⁻¹, respectively. The energies of adsorption was calculated as

$$E_{Ads} = (E_{Surf+adsorbate} - E_{Surf} - E_{adsorbate})/2$$

where $E_{Surf+adsorbate}$, E_{Surf} , and $E_{adsorbate}$ are the energies of the adsorbates adsorbed onto the surface, of the bare surface, and of the isolated adsorbate, respectively, and 2 accounts for the adsorption of the adsorbates on both sides of the slab.

2.2. Virus Studies

2.2.1 Cells and Viruses

Cultures of HeLa cells were grown in Dulbecco modified Eagle medium (DMEM, Gibco, Thermo Fisher Scientific) supplemented with 10% heat-inactivated fetal calf serum (HI FBS, Gibco, Thermo Fisher Scientific). Human Rhinovirus 14 (RV14, ATCC, catalog number VR-284) was grown in HeLa cells at 33°C. RV14 stocks were determined by a TCID₅₀ assay using confluent HeLa cells as described previously(36). Briefly, virus stock was serially diluted in DMEM containing 10% Bovine Serum Albumin (BSA 7.5% solution, Gibco, Thermo Fisher Scientific) as carrier protein. Cells were incubated with diluted virus solutions for one hour at 33°C. Cells were then washed, replaced with DMEM containing 2% HI FBS, and incubated at 33°C for 3 days. Cells were stained with a crystal violet solution and TCID₅₀ units were calculated by the Spearman & Kärber algorithm as previously described(55). The Orsay strain of vesicular stomatitis virus (VSV) was grown in Vero cells at 37°C for 2 days and VSV stocks were determined by TCID₅₀ assay using confluent HeLa cells as described above.

2.2.2 AgCNP-Resistant Rhinovirus Selection.

AgCNP-resistant (AgCNP2 from previous study (36), AgCNPctrl hereafter) RV14

was generated as described previously (35). Briefly, ~5×10⁵ TCID₅₀ units of parental RV14 was incubated with 0.1 mg/mL AgCNPctrl for 1 hr. Reactions were then diluted in DMEM containing 0.38% BSA and used to generate a virus stock in HeLa cells. These cycles of treatment and expansion were repeated for a total of 3 selection rounds with a nanoparticle concentration of 0.1 mg/mL. AgCNPctrl concentration was then adjusted to 0.2, 0.1, and 0.15 mg/mL for the 4th, 5th, and 6th selection rounds, respectively. After the 6th round, RV14 was harvested and pelleted as described above.

2.2.3 Nanoparticle Virus Inactivation Assays

Nanoparticles were prepared and studies in liquid were performed as previously reported(36). Briefly, nanoparticles were ultrasonicated, diluted in inactivation buffer to the desired concentration as indicated in the figure legends, and incubated with virus at room temperature. After indicated incubation times, remaining infectious virus was quantified by TCID₅₀ as described above.

2.2.4 Statistical Analyses.

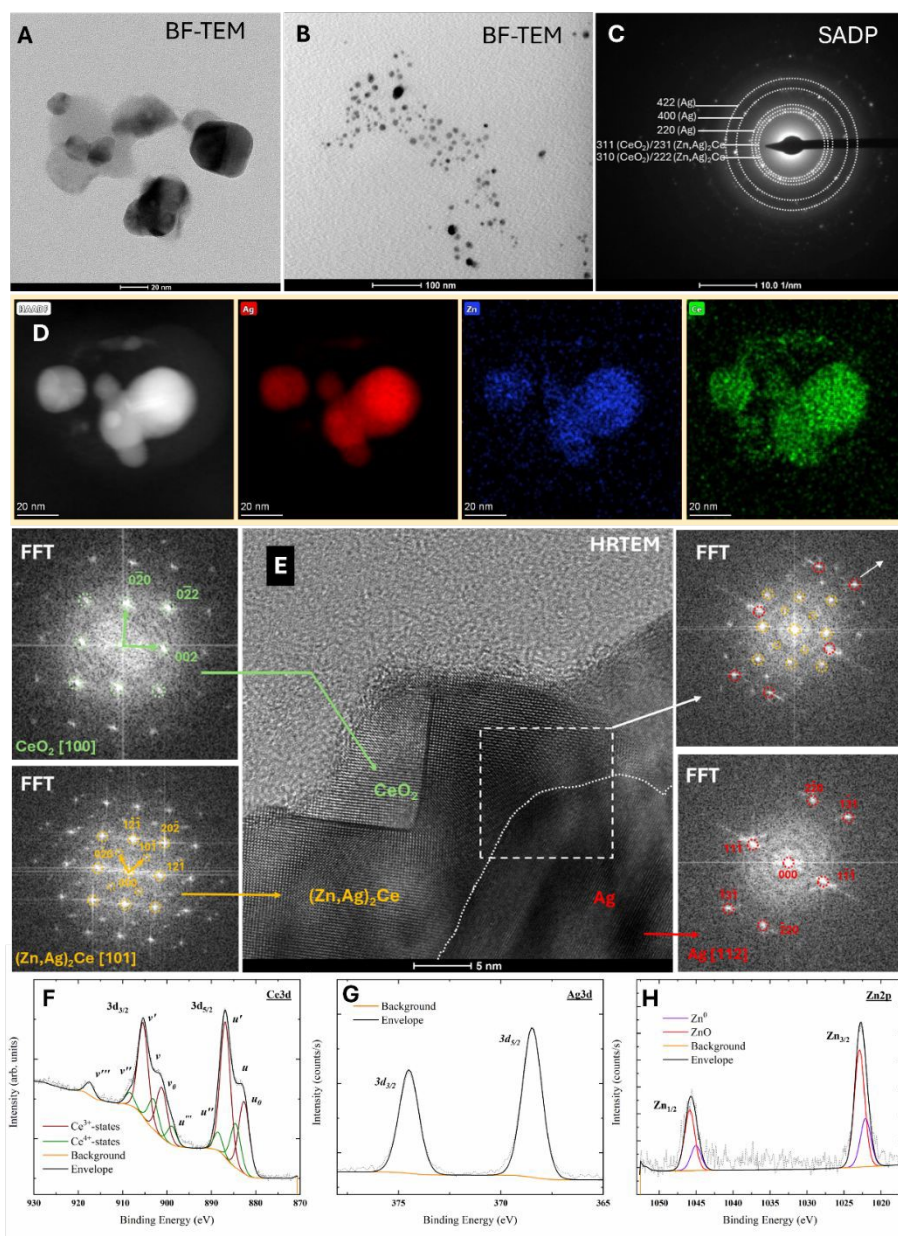
Unless otherwise indicated, values are the mean of three independent samples, with error bars representing the standard deviation. Statistical analysis was performed using GraphPad ordinary one-way ANOVA comparing untreated 1hr samples to the nanoparticle treated samples. In all figures, * indicates a p-value of <0.05, ** indicates p-value of <0.01, and *** indicates a p-value of <0.001.

2.3. Bacterial Studies

2.3.1 Bacterial Studies Minimum inhibitory concentration (MIC) determination for Ag/Zn-CNP

The minimum inhibitory concentration (MIC) of Ag/Zn-CNP was determined in Tris buffer (25 mM Tris/75 mM NaCl; Tris-NaCl) and in Luria-Bertani (LB) broth. The lowest concentration of Ag/Zn-CNP that inhibits bacterial growth was measured for *P. aeruginosa* ATCC 15442 (Gram negative), *S. aureus* ATCC 6538 (Gram positive), and methicillin-resistant *S. aureus* ATCC 33592 (MRSA) in Tris-NaCl and LB media at pH 7.2. Bacterial inoculums were adjusted to 10⁸ CFU/mL. Tris-NaCl and LB media inoculated only with 10⁸ CFU/mL bacteria were used as controls. MICs were determined by broth dilution using a 96-well flat-bottom microtiter plate. Final Ag/Zn-CNP concentrations of 2, 4, 6, 8, and 10 µg/mL were prepared in Tris-NaCl medium for all three bacterial strains. In LB medium, final concentrations of 10, 20, 30, 40, 50, 60, 70, 80, and 100 µg/mL were tested for *P. aeruginosa*, while 10, 20, 30, 40, 50, 60, 70, 80, 100, 200, 300, and 400 µg/mL were tested for *S. aureus* and MRSA. Cultures were incubated at 37 °C with shaking at 210 rpm for 24 h, and changes in optical density at 600 nm were used to assess bacterial growth in LB medium. Gentamicin was included as a study control group.





View Article Online
DOI: 10.1039/D5NR05105C

Figure 1. Materials Characterizations of Silver-Zinc Cerium Oxide Nanoparticles. A bright-field transmission electron microscopy (BF-TEM) image taken at higher magnification showing a morphology of some of the observed nanoparticles (A) together with a micrograph recorded at lower magnification (B) showing a distribution of the observed nanoparticles. The selected area diffraction pattern (SADP) taken from larger area indicating presence of different types of nanoparticles (C) together with the Scanning Transmission Electron Microscopy High-Angle Annular Dark Field (STEM-HAADF) image with results of elemental mapping indicated intermixing of cerium, silver and zinc in the observed area (D). High-Resolution Transmission Electron Microscopy (HRTEM) image with Fast Fourier Transforms (FFT) from selected regions showing the details of structure and symmetry of the observed nanoparticles. The d – values obtained from HRTEM images (E) suggest the formation of Zn-rich compounds. X-ray photoelectron spectroscopy (XPS) measurements with binding energy regions for Ce3d (F), Ag3d (G), and Zn2p (H) chemical states. Peak fittings to Ce³⁺ and Ce⁴⁺ states provide insight into the density of oxygen vacancies at the material surface and thereby their unique redox chemistry. Interestingly, silver (G) content in the nanoparticle formulation is observed in a metallic state while zinc (H) occurs in both metallic and oxide states. The range of component valencies may also contribute to observed antimicrobial activities via associated redox reactions such as the generation of free radicals by engineered nanoceria formulations.

2.3.2 Time scale study To carry out a time course assay, bacterial inoculums were adjusted to 10^8 CFU/mL in protein-free medium, Tris-NaCl. The MIC of Ag/Zn-CNP (4 μ g/mL for *P. aeruginosa* and 6 μ g/mL for *S. aureus* and MRSA) was evaluated in a final volume of 25 mL. Control groups included bacteria with (i) no treatment and (ii) 20 μ g/mL gentamicin. The cultures were then incubated at 37 °C under agitation (210 rpm). 50 μ L from each of the treated samples were spread onto LB agar plates, and growth was assessed at 15, 30, 45, 60, and 75 minutes for

P. aeruginosa, and at 60, 120, 180, and 240 minutes for *S. aureus* and MRSA. Colony-forming units (CFU/mL) were quantified after incubation at 37 °C for 16 h.

2.3.3 Effect of temperature on Ag/Zn-CNP activity Bacterial inoculums were adjusted to 10^8 CFU/mL, and a time-course study was carried out in Tris-NaCl medium. The MIC of Ag/Zn-CNP (4 μ g/mL for *P. aeruginosa* and 6 μ g/mL for *S. aureus* and MRSA) was evaluated at a final volume of 10 mL. Cultures



without Ag/Zn-CNP served as the control group and all cultures were incubated at 4 °C under agitation at 210 rpm. Aliquots (50 µL) were spread onto LB agar plates, and growth was assessed after 1 and 24 h for *P. aeruginosa*, and after 3 and 24 h for *S. aureus* and MRSA. Colony-forming units (CFU/mL) were quantified following incubation at 37 °C for 16 h.

2.3.4 Resistance-development towards Ag/Zn-CNPs

Approximately 10⁸ CFU/mL of *P. aeruginosa* and *S. aureus* were incubated in LB medium at their sublethal (IC₅₀) concentrations of Ag/Zn-CNP, corresponding to 20 µg/mL and 200 µg/mL, respectively. Culture grew at 37°C at 210 rpm for 2 hr. Then 50 µL of culture was plated onto an LB agar plate and incubated overnight at 37 °C. A single colony from each plate was then reinoculated into LB medium and exposed again to the IC₅₀ concentration of Ag/Zn-CNP. This treatment cycle was repeated eight times. After the 6th and 8th cycles, *P. aeruginosa* and *S. aureus* were tested for resistance development by exposing them to their MIC values of Ag/Zn-CNP (30 µg/mL and 400 µg/mL, respectively) under the culture conditions of 37°C and 210 rpm for 16 hours. Cultures were consequently plated onto LB agar and examined for resistant colonies.

2.3.5 Bactericidal effect of Ag/Zn-CNP on resistant strains

The effect of Ag/Zn-CNP was studied against the AgCNP-resistant strains *P. aeruginosa* and *S. aureus* (laboratory strain). 10⁸ CFU/mL of bacteria were treated with increasing concentrations of Ag/Zn-CNP in Tris-NaCl (10, 20, 30, 40, 50, and 60 µg/mL) at 37 °C for 24 hours. 50 µL of the tested samples were plated onto the LB agar and incubated overnight at 37 °C. Grown colonies were counted and recalculated to the number of CFU/mL.

2.3.6 Effect of Ag/Zn-CNP on cell metabolic activity on macrophage cells

The cells were maintained in Dulbecco's Modified Eagle Medium (DMEM; Thermo Fisher Scientific, USA) supplemented with 10% heat-inactivated fetal bovine serum (FBS; Thermo Fisher Scientific, USA), 1% (v/v) penicillin–streptomycin (P/S; Thermo Fisher Scientific, USA), and 2 mM L-glutamine. Cultures were kept in a humidified incubator at 37 °C with 5% CO₂. Cell metabolic activity was assessed on days 1 and 3 using an MTT assay [3-(4,5-dimethylthiazol-2-yl)-2,5-diphenyltetrazolium bromide] (M2128, Millipore Sigma, USA). RAW 264.7 macrophages were seeded in 96-well plates at a density of 2.5x10⁴ cells/well and cultured at 37 °C with or without Ag/Zn-CNP at concentrations of 4, 6, 30, 100, or 400 µg/mL. On the designated culture days, 20 µL of a 5 mg/mL MTT solution was added to each well and incubated for 4 h. The supernatant was then carefully removed, and 100 µL of dimethyl sulfoxide (DMSO) was added to dissolve the resulting formazan crystals. Absorbance was measured using a SpectraMax iD3 multimode microplate reader (Molecular Devices, CA, USA).

2.3.7. Statistical Analyses.

All bacterial experiments were carried out in triplicate. Data is presented as mean±standard

error. Statistical analysis was performed using two-way ANOVA with a post-hoc Tukey's test for comparison between groups (GraphPad Prism, v8, USA). *p* values <0.05 were considered significant.

3. Results and Discussion

3.1 Synthesis of Ag/Zn-CNP formulation

Silver and zinc surface phase modified cerium oxide nanoparticles (Ag/Zn-CNPs) were synthesized by treating an aqueous solution of Ag⁺, Zn²⁺, and Ce³⁺ nitrates with hydrogen peroxide, followed by ageing for 8-weeks. During this ageing period, similar to our observations for pure cerium oxide and silver-cerium oxide nanoparticle formulations produced by comparable methods, the solution coloration went from dark yellow-orange to pale yellow and finally to colorless. This cycling from clear to orange and back to a clear solution has been ascribed to redox cycling of Ce³⁺/Ce⁴⁺ and to the formation/degradation of cerium peroxy, as well as oxyhydroxy, complexes, as previously reported for pure cerium nitrate-hydrogen peroxide systems. Additionally, a precipitate formation was observed, with a spontaneous re-dispersion occurring over the ageing period: also observed for comparable pure cerium and cerium-silver nitrate systems. The extended ageing period is ascribed to the slow kinetics of peroxide oxidation of cerium at the low pH of the synthesis (~3.5) and the absence of observable (*i.e.*, *via* black/brown coloration), or measured (*vide infra*; Fig. 1I), silver oxide tentatively to the presence of free peroxide ($Ag_2O + H_2O_2 \rightarrow 2Ag + H_2O + O_2$).

3.2 Materials Characterization of Silver/Zinc-Cerium Oxide Nanoparticles

3.2.1 Microscopy and Phase composition

TEM observations (Fig. 1) confirmed the presence of small, aggregated clusters of spherical-shaped nanoparticles with a mean diameter of 11 nm (Fig. 1A-B). The EDX elemental mapping indicated intermixing of cerium, silver and zinc within them (Fig. 1D). Literature data on the thermodynamic equilibrium in the Ag-Ce-Zn system are very scarce, and, as expected, even less is known regarding the oxide combinations of these metals. However, in the study of Long et al. on the thermodynamics of Ag-Ce-Zn, the isothermal cross-sections have been calculated and experimentally verified for 450 and 600 °C (56). It has been shown that Ag₂Ce and Zn₂Ce phases can be combined as (Ag,Zn)₂Ce because of their mutual solubility. Ag₂Ce phase (Pearson symbol of oI12, space group Imma), possess the lattice parameters of a=0.48nm, b=0.709 nm, c= 0.82 nm (57), while Zn₂Ce phase lattice parameters (and the same space group as Ag₂Ce) are very similar and as follows: a=0.4633 nm, b=0.7538 nm, c=0.749 nm (58). Therefore, for the electron diffraction pattern taken from the larger area, beside the presence of silver nanoparticles (AgNPs) also (Zn,Ag)₂Ce phase has been identified (Fig. 1C). Cerium oxide has a cubic structure with *Fm* $\bar{3}$ *m* space group (lattice parameter: a=0.547 nm), where Ce⁴⁺ is bonded to eight equivalent O₂⁻ atoms, while O₂⁻ is bonded to four equivalent Ce⁴⁺. On the other hand, silver has the same structure as CeO₂ (cubic with *Fm* $\bar{3}$ *m* space group) with a lower lattice parameter a=0.41 nm. It is also



worthy of mention that silver is able to dissolve relatively high amounts of zinc (up to 20 at.%) without changing its structure

formulation's phase composition and provide potential insight into later detailed biomedical properties/behaviors.

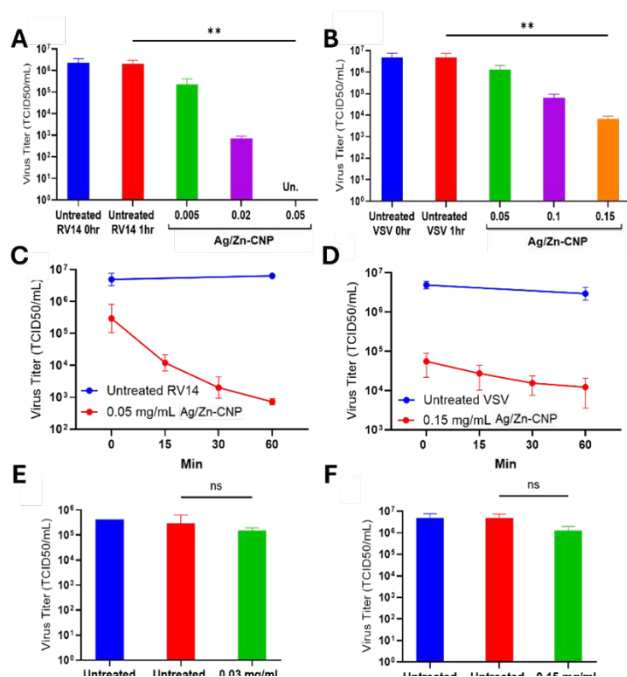


Figure 2. Effect of 77WC-1 and AgCNP3 Nanoparticles on RV14 and VSV Infectivity. Liquid reactions of virus and nanoparticles were incubated at room temperature for 1hr. Nanoparticle and virus reactions were collected at 1hr post nanoparticle addition while untreated virus controls were collected at 0hr and 1hr. Remaining infectious virus titer was determined by TCID₅₀ assay. A and B) increasing concentrations of 77WC-1 nanoparticles or buffer alone were incubated with RV14 (A) or VSV (B) then assayed for remaining infectious virus. C and D) 0.05 mg/mL of 77WC-1 was incubated with RV14 (C) or VSV (D), respectively. Samples were collected at 0, 15, 30, and 60 min and TCID₅₀ assay was used to quantify infectious virus in each sample. E and F) AgCNP3 nanoparticles were incubated with RV14 (E) or VSV (F) at concentrations of 0.03 mg/mL or 0.15 mg/mL, respectively, for 1hr at room temp then collected to quantify infectious viruses. Values in all panels are the mean of three replicates with error bars representing standard deviation.

(59). During the TEM studies it was found that Zn-containing particles (Zn,Ag)₂Ce (see example in Fig. 1E) are not stable under an electron beam causing difficulties in data acquisition.

Kourouklis *et al.* have studied ceria pressure phase transformation up to 35 GPa and by registering the Raman spectra they observed this phenomenon near 31 GPa, when the structure of CeO₂ has changed from the above-mentioned fluorite-type to the so-called cottunite (PbCl₂ type, orthorhombic *Pnma*) (60). However, in our case, phase parameters fitted to the cubic structure of ceria (Fig. 1C); therefore, both ceria and (Zn,Ag)₂Ce are marked as possible phases. High-Resolution Transmission Electron Microscopy (HRTEM) observations evidenced the presence of silver, (Zn,Ag)₂Ce and CeO₂ compounds (Fig. 1E). The structure and symmetry of the observed nanoparticles were confirmed by Fast Fourier Transforms (FFT) collected from the selected regions showing ceria NP of cubic symmetry oriented along [001] axis, AgNPs along [112] and (Zn,Ag)₂Ce located in between them and oriented along the [101] axis. Chemical state analysis was also performed for particle samples to further assess the

3.2.2 Chemical State Composition Analysis of Silver/Zinc-Cerium Oxide Nanoparticles

X-ray photoelectron spectroscopy (XPS) was performed (Fig. 1) with analysis focused primarily on the Ce3d, Ag3d, and Zn2p binding energy regions (Figs. 1B, C, and D, respectively). Curve fitting was performed for all spectra over measured signal envelopes using peaks chosen by reference to relevant literature and database (*Thermo Scientific Avantage Data System*). The fitted spectra in the Ce3d region are reflective of the mixed valence state (Ce³⁺/Ce⁴⁺) typically observed for cerium oxide. Peaks attributed to each of the formal oxidation states are presented in Fig. 1G. Semi-quantitative analysis, performed through summation over area-under-the-curve calculations for specific chemical states

$$\%Ce^{3+} = 100 * \frac{\sum \int \{u_0, v_0, u', v'\}}{\sum \int \{All Fitted Peaks\}}$$

where u_0 , v_0 , u' , and v' represent Ce³⁺-associated states and the calculated percentage is with respect to the total measured population of cerium state related signal peaks (*All Fitted Peaks*), suggests a significant (calculated %Ce³⁺ = 51.18) population of Ce³⁺-associated states for the Ag/Zn-CNPs formulation. This relatively high percentage of reduced chemical state cerium sites is characteristic of this synthesis: with previous investigations of pure and of silver-modified cerium oxide nanoparticle formulations being similarly rich in Ce³⁺ (61) (62) (63). For silver-modified cerium oxide materials, Ce³⁺ states have been observed in published experimental studies at higher densities at silver-cerium oxide interfaces, with related theoretical investigations noting a greater stability for silver ions at surface Ce³⁺-sites. Similar to our previous findings for a silver-modified cerium oxide nanoparticle formulation (previously reported as AgCNP2), signal in the Ag3d region is well-described by fitting to a metallic silver (Ag⁰)-associated doublet (Fig. 1H). Interestingly, signal envelope peaks in the Zn2p binding energy region show an asymmetry, with fitted doublets related to metallic (Zn⁰) and cationic (Zn²⁺) states approximating the measurement curve (Fig. 1I). The determined chemical state distributions for silver and zinc appear to corroborate findings from HRTEM analysis; specifically, the presence of larger silver nanoparticles and more complex (Ag,Zn)₂Ce compound phases. However, it should also be noted that other studies have identified silver oxide interphase regions directly at silver-ceria interfaces; therefore, we should consider that these XPS measurements do not capture the total chemical state distribution of material components in complete detail. It is possible that oxide states for silver exist in minority populations, are not discernible in our collected XPS spectra, though they may contribute to catalytic behaviors.

We next considered the antimicrobial efficacy of this synthesized Ag/Zn-CNP formulation towards assorted virus (enveloped vesicular stomatitis virus, non-enveloped RV14 rhinovirus) and bacteria (Gram-positive *S. aureus*, methicillin-resistant *S. aureus*; Gram-negative *P. aeruginosa*) species.

3.3 Virus Studies



3.3.1 Silver/Zinc Cerium Oxide Nanoparticles Display Potent Antiviral Activity Against Rhinovirus and Vesicular Stomatitis Virus.

To determine the extent to which silver-modified CNPs, prepared by a comparable synthesis approach and reported previously, (AgCNPctrl) or Ag/Zn-CNPs inactivate rhinovirus (RV14) or vesicular stomatitis virus (VSV), aqueous solutions of nanoparticles and virus were incubated together for 1hr. Remaining infectious virus was determined by 50% tissue culture infection dose (TCID₅₀) assay. Here, we show that Ag/Zn-CNPs inactivate RV14 in a dose-dependent manner, with 0.05 mg/mL reducing the remaining virus titer to beyond detectable ranges (Fig. 2A). Ag/Zn-CNPs also demonstrate dose-dependent inactivation of VSV (Fig. 2B). However, it is notable that higher concentrations of Ag/Zn-CNPs are necessary to achieve the same log reduction in virus titer in VSV versus RV14. Time-course studies show rapid anti-viral activity of Ag/Zn-CNPs against RV14 (Fig. 2C) and VSV (Fig. 2D), with greater than 50% total virus inactivation occurring within 15 min. The effective concentrations of Ag/Zn-CNPs were used to compare the antiviral activity of Ag/Zn-CNPs versus AgCNPctrl. The above finding that Ag/Zn-CNPs concentrations of 0.02 mg/mL and 0.15 mg/mL reduced > 50% infectivity of RV14 and VSV, respectively, contrasts with results in Fig. 2E and 2F showing treatment with concentrations of 0.03 mg/mL and 0.15 mg/mL of AgCNPctrl being ineffective at inactivating RV14 and VSV, respectively. Taken together, these data demonstrate that Ag/Zn-CNPs rapidly inactivate RV14 and VSV at lower concentrations than the previous nanoparticle formation, AgCNPctrl.

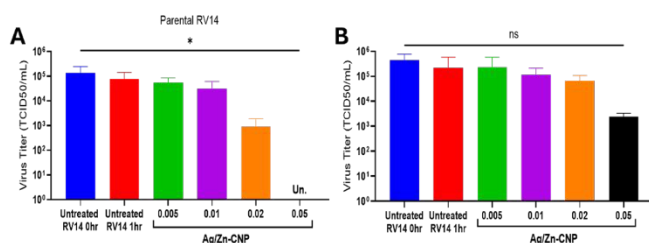


Figure 3. Antiviral Activity of Ag/Zn-CNPs against AgCNP-Resistant RV14. AgCNP-Resistant RV14 was generated as described previously(35). Liquid reactions of parental or AgCNP-resistant RV14 and nanoparticles were incubated at room temperature for 1hr. Nanoparticle and virus reactions were collected at 1hr post nanoparticle addition while untreated virus controls were collected at 0hr and 1hr. Remaining infectious virus titer was determined by TCID₅₀ assay. A and B) increasing concentrations of Ag/Zn-CNP nanoparticles or buffer alone were incubated with parental RV14 (A) or AgCNP-resistant RV14 (B) then assayed for remaining infectious virus. Values in all panels are the mean of three replicates with error bars representing standard deviation.

3.3.2 Ag/Zn-CNPs Demonstrate Antiviral Activity Against AgCNP-Resistant RV14. AgCNP-resistant RV14 was previously generated via sequential rounds of exposure to suboptimal AgCNP and was shown to gain resistance to AgCNP inactivation (35). To determine the extent to which Ag/Zn-CNPs inactivate AgCNP-resistant RV14, aqueous solutions of nanoparticles and virus were incubated together for 1hr. Remaining infectious virus was determined by 50% tissue culture infection dose (TCID₅₀) assay. Here, we show that Ag/Zn-CNPs inactivate parental RV14 in a

dose-dependent manner, with 0.05 mg/mL reducing the remaining virus titer to beyond detectable ranges (Fig. 3A). Ag/Zn-CNPs also demonstrate dose-dependent inactivation of AgCNP-Resistant RV14 (Fig. 3B), with 0.05 mg/mL resulting in a 2-log reduction in virus titer. Notably, the log reduction in resistant-RV14 is considerably less than that observed in the parental virus, suggesting that AgCNP-resistant RV14 might be partially resistant to Ag/Zn-CNPs inactivation. Together, these data demonstrate that Ag/Zn-CNPs display antiviral activity against AgCNP-resistant RV14, although higher doses of nanoparticle might be necessary to inactivate resistant virus.

3.4 Bacterial Studies

3.4.1 Silver/Zinc-Cerium Oxide Nanoparticles in Absence of Protein.

P. aeruginosa, *S. aureus*, and MRSA when treated with Ag/Zn-CNP in a simple 25 mM Tris/75 mM NaCl buffer medium, containing no potentially surface-fouling biomolecules, caused a concentration-dependent reduction in bacterial viability (Fig. 4A-C, respectively). When all three bacterial species were exposed to Ag/Zn-CNP, this resulted in a significant decrease in CFU/mL compared with the untreated controls with complete eradication measured at a dose >2 μg/mL in the *P. aeruginosa* group ($p < 0.0001$) and >4 μg/mL in the *S. aureus* and MRSA groups ($p < 0.0001$). The MIC for *P. aeruginosa*, was found to be ~4 μg/mL, and treatment with 2 μg/mL resulted in an ~3-log reduction in CFU/mL relative to the control. *S. aureus* showed a similar trend, with an MIC of approximately 6 μg/mL. Notably, MRSA exhibited the greatest susceptibility to Ag/Zn-CNP when compared to gentamicin with an MIC of approximately 6 μg/mL. Even in the presence of gentamicin (20 μg/mL), only a ~3-log reduction in CFU/mL was observed for MRSA when compared with the untreated group. The results indicate that Ag/Zn-CNPs have a potent bactericidal effect against both Gram-negative and Gram-positive bacteria, including antibiotic-resistant MRSA.

3.4.2 Silver/Zinc-Cerium Oxide Nanoparticles in Presence of Protein.

The antibacterial efficacy of Ag/Zn-CNP was investigated against *P. aeruginosa*, *S. aureus*, and MRSA when cultured in protein-rich LB medium (Fig. 4D-F, respectively). A dose-dependent decrease in bacterial growth was observed in all three strains. *P. aeruginosa* growth was significantly reduced at Ag/Zn-CNP concentrations >20 μg/mL ($p < 0.0001$). Similarly, *S. aureus* and MRSA growth were significantly reduced at concentrations >10 μg/mL and >20 μg/mL ($p < 0.05$) respectively. However, it is notable that MIC values measured in LB broth were significantly lower than those measured for protein-free buffer medium. It is proposed that this difference is partly ascribable to fouling of the material surface by biomolecule adsorption. Modification of the material surface can alter surface chemistry, including enzyme-mimetic redox reactions shown previously to contribute to antimicrobial performance, as well as function as a physical barrier between nanoparticle and environment. The greatest observed efficacy was towards



the Gram-negative *P. aeruginosa* viability, with an MIC of around 30 $\mu\text{g/mL}$, while MIC values for the Gram-positive *Staphylococcus* strains were markedly higher at $\sim 400 \mu\text{g/mL}$. Interestingly, this trend in Gram positive versus negative bacteria inactivation was previously observed, for the same bacterial strains, for AgCNPs produced by a comparable synthesis (1).

3.4.3 Bacterial Inactivation Kinetics A time-dependent study of bacteria inactivation by Ag/Zn-CNPs was performed for all three bacterial strains at their respective MIC values (4 $\mu\text{g/mL}$ for *P.*

aeruginosa over the *Staphylococcus* strains held for these kinetic studies: with complete bacterial elimination occurring by 180 minutes (*S. aureus*, Fig. 4H; MRSA, Fig. 4I). Ag/Zn-CNP nanoparticles demonstrated rapid and potent bactericidal activity across all tested species in Tris-NaCl medium, outperforming gentamicin. To further evaluate Ag/Zn-CNPs' utility as a potent antimicrobial agent, we next examined the potential for a resistant strain to be developed.

3.4.4 Probe of Resistance-development following repeated-use testing towards Ag/Zn-CNPs Repeated exposures of *P.*

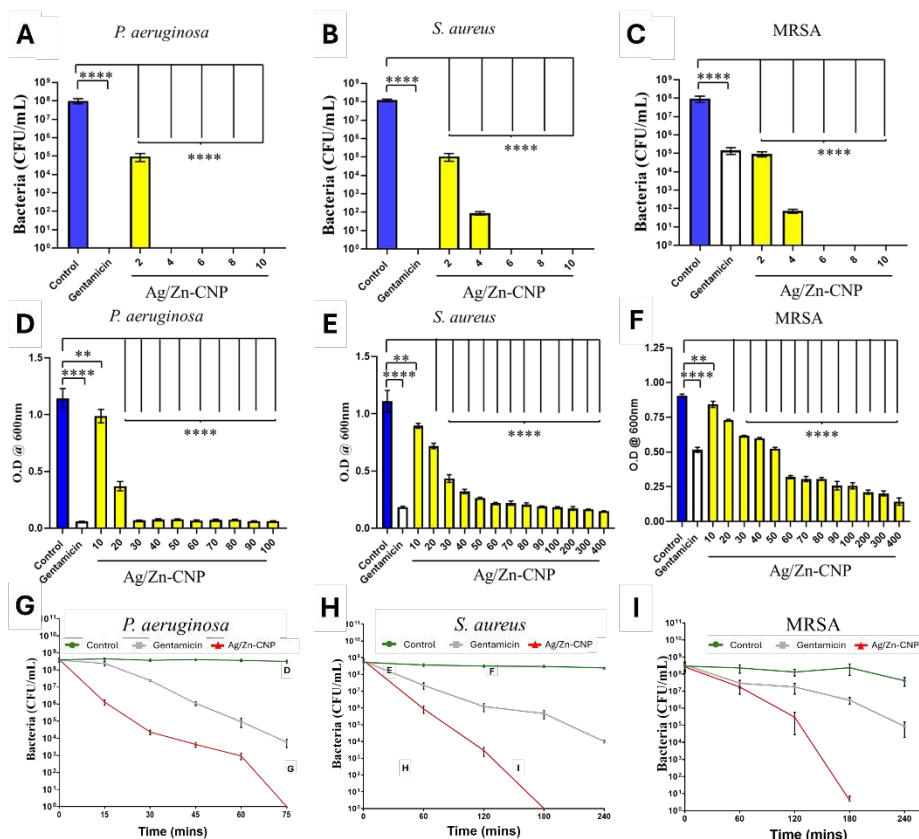


Figure 4. Bactericidal Efficacies of Ag/Zn-CNP against *P. aeruginosa*, *S. aureus* and MRSA and Time-dependent Studies. Each bacterial strain was suspended in Tris-NaCl, pH 7.5 and treated with increasing concentrations of Ag/Zn-CNP and gentamicin (20 $\mu\text{g/mL}$) in a 96-well microtiter plate before being incubated for 24 hours at 37 $^{\circ}\text{C}$ (A-C). The MIC values of Ag/Zn-CNP were found to be 4 $\mu\text{g/mL}$ for *P. aeruginosa* (A), 6 $\mu\text{g/mL}$ for *S. aureus* (B), and 6 $\mu\text{g/mL}$ for MRSA (C). Nanoparticle efficacy towards these strains at $\sim 10^8$ CFU/mL were further tested in Luria-Bertini (LB) broth and compared against gentamicin (20 $\mu\text{g/mL}$) in a 96-well microtiter plate, followed by incubation at 37 $^{\circ}\text{C}$ for 24 h. The MIC values of Ag/Zn-CNP were determined to be 30 $\mu\text{g/mL}$ for *P. aeruginosa* (D), 400 $\mu\text{g/mL}$ for *S. aureus* (E), and for MRSA (F). Experiments for both sets of studies were carried out in triplicate and data is presented as mean \pm standard error. * $p < 0.05$, ** $p < 0.01$, *** $p < 0.001$, and **** $p < 0.0001$. Growth curves for control, gentamicin (20 $\mu\text{g/mL}$) and Ag/Zn-CNP at respective MIC concentration for each bacteria. When tested at the MIC of Ag/Zn-CNP, an ~ 7 -log reduction was seen in each group: exceeding the EPA minimum requirement for an antibacterial product.

aeruginosa; 6 $\mu\text{g/mL}$ for *S. aureus* and MRSA) in Tris-NaCl medium. A progressive and rapid reduction in viable bacteria was seen for all three bacterial species when treated with Ag/Zn-CNP; whereas the effects of gentamicin occurred at a significantly slower rate for all tested strains (only reaching 4, and 3 -log reductions for *P. aeruginosa*, *S. aureus*, and MRSA, respectively, by times of complete inactivation for Ag/Zn-CNPs). For *P. aeruginosa* (Fig. 4G), a complete inhibition of bacteria by Ag/Zn-CNP was observed by 75 minutes, whereas cells treated with gentamicin saw only a 5-log reduction within the same time period. Interestingly, the observed trend of greater

aeruginosa and *S. aureus* to sub-lethal concentrations (IC_{50}) of Ag/Zn-CNPs was performed and their susceptibilities at respective, previously determined, MIC values analyzed. Bacteria were exposed to eight sequential sub-lethal exposure and re-culture cycles, with potential resistance development evaluated by treating sub-cultures at the 6th (Fig. 5A,C) and 8th (Fig. 5B,D) cycles at their respective MIC values in LB medium. Across the studied bacterial species, no substantial increase in tolerance or survived cells were detected in the presence of Ag/Zn-CNP (Fig. 5): suggesting no appreciable tendencies towards development of phenotypic resistance, even after



multiple cycles of exposure. However, it was found in performing a similar study that lab strains of AgCNP-resistant *P. aeruginosa* and *S. aureus* could be produced. In a follow-on study, we examined the susceptibility of these AgCNP-resistant strains towards Ag/Zn-CNPs.

3.4.5 Susceptibility of AgCNP-resistant strain to Ag/Zn-CNP nanoparticle in Tris-NaCl. On treatment with Ag/Zn-CNPs, AgCNP-resistant *P. aeruginosa* and *S. aureus* (laboratory) strains experienced dose-dependent decreases in viability. For both bacteria species, the measured MIC values for parental strains (Figs. 5E and G, ~4 and 6 $\mu\text{g/mL}$, for *P. aeruginosa* and *S. aureus*, respectively) were significantly lower ($p < 0.0001$) than those

and H, ~50 and 60 $\mu\text{g/mL}$, for *P. aeruginosa* and *S. aureus*, respectively) suggesting some increase in bacterial robustness towards Ag/Zn-CNP exposure as well as demonstrating a persistent antimicrobial efficacy for the Ag/Zn-CNP formulation. The overall susceptibility of Gram-positive *Pseudomonas* was slightly lower than that of Gram-negative *Staphylococcus*.

3.5 Antimicrobial Function Discussion

In our previous studies of AgCNP formulations towards viruses and bacteria, an initial probe into respective mechanisms of antimicrobial action was performed. Treatment of an enveloped parainfluenza virus (PIV5; negative-sensed, single-stranded RNA virus) with AgCNP (AgCNP_{ctrl} in the present study) induced an aggregation of virions, suggested by a dose-dependent decrease in hemagglutination of red blood cells by NP-treated PIV5 inocula, and by gradient centrifugation studies. Importantly, this observation of NP-induced virus aggregation in centrifugation occurred without appreciable segregation of virions to lower density gradient bands. This observation allows an important insight: specifically, that the dominant mechanism of virus inactivation is likely not binding protein, or general surface, degradation/modification due to disruption of the integrity of the virus particle, but rather that the NPs bind virus surface sites and inhibit an early stage in infection. In the same study, a lab strain of non-enveloped rhinovirus (RV14; single-stranded, positive-sensed RNA virus) was produced which was found to be substantially less sensitive to AgCNP_{ctrl} than the parental strain. Genomic analysis identified five point mutations, two of which induced changes in amino acid identity (the other three being silent mutations in VP3 protein encoding region) and both in a superficial/exterior region of a surface binding protein subunit (VP1). While these findings are not direct evidence, the loss of virus inactivation and the presence of amino acid mutations which converted hydrophilic to hydrophobic amino acid expressions implicate these proteins in the virus inhibition mechanism. Our prior work (3) showed that AgCNP-treated viruses had lost receptor binding. It is possible that the ability of Ag/Zn-CNPs to bypass AgCNP-resistance reflects i) prolonged interactions of Ag/Zn-CNPs with virions, ii) improved access of Ag/Zn-CNPs to the virus receptor binding domain, or iii) higher denaturation of viral capsid proteins leading to increased virus aggregation and/or blocks in uncoating of virus during infection.

Corresponding studies of AgCNP_{ctrl} treatments on bacterial species (*P. aeruginosa*, *S. aureus*, MRSA) evidence effects from reactive oxygen species (ROS) generation, DNA damage, modulation of cellular oxygen metabolism, and particle adsorption on cell viability(1). For all tested bacteria, cell lysis was observed. Interestingly, despite the apparent multitude of contributing antibacterial mechanisms, results from the present study further demonstrate the potential to produce AgCNP-resistant strains of *P. aeruginosa* and of *S. aureus*. Ag/Zn-CNPs retain antibacterial activity towards these strains: suggesting an incomplete overlap in the dominant mechanisms producing the antibacterial outcome. Measurements of antibacterial

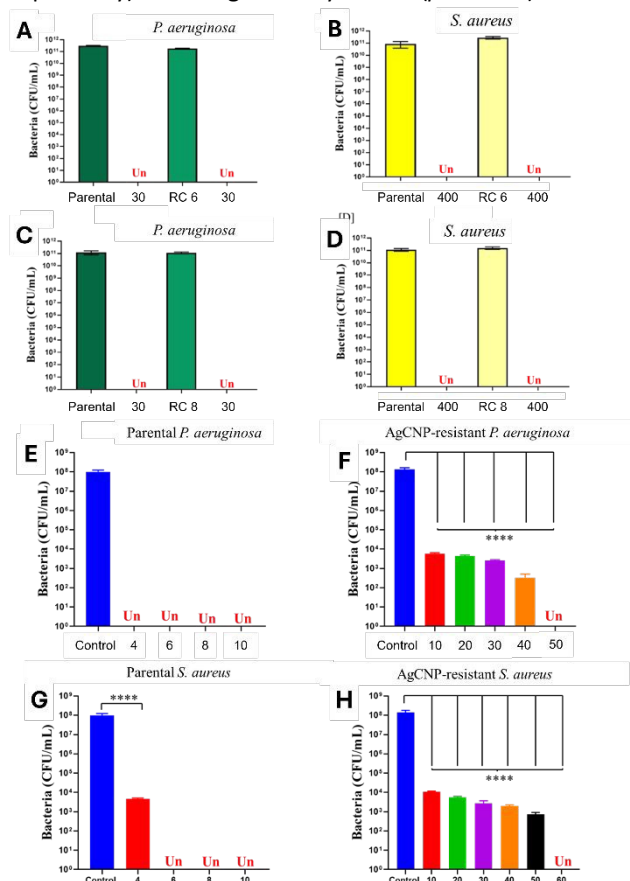


Figure 5. Resistance development to Ag/Zn-CNP NP assessed after repeated exposure rounds in LB medium. (A, C) Parental *P. aeruginosa* and *P. aeruginosa* cells are isolated after 6th (RC 6) and 8th (RC 8) cycle were treated with Ag/Zn-CNP of 30 $\mu\text{g/mL}$ (MIC). Cells are undetected (Un) after 24 hours of treatment in both phenotypes. (B, D) Parental *S. aureus* and *S. aureus* cells are isolated after 6th (RC 6) and 8th (RC 8) cycle were treated with Ag/Zn-CNP of 400 $\mu\text{g/mL}$ (MIC). Cells are undetected (Un) after 24 hours of treatment in both phenotypes. Thus, demonstrating that when cells are repeatedly exposed to Ag/Zn-CNP it did not induce resistance development. Antibacterial activity of Ag/Zn-CNP against parental and AgCNP resistant *P. aeruginosa* and *S. aureus*. (A, C) Parental *P. aeruginosa* and *S. aureus* strains treated with Ag/Zn-CNP (4, 6, 8 and 10 $\mu\text{g/mL}$). Cells are undetected (Un) after treating them with 4 $\mu\text{g/mL}$ in *P. aeruginosa* and 6 $\mu\text{g/mL}$ in *S. aureus*. (B, D) AgCNP resistant *P. aeruginosa* and *S. aureus* treated with Ag/Zn-CNP (10, 20, 30, 40, 50 and, 60 $\mu\text{g/mL}$). Cells are undetected (Un) at 50 $\mu\text{g/mL}$ in *P. aeruginosa* and 60 $\mu\text{g/mL}$ in *S. aureus*. The results are shown as mean \pm standard error, and the experiments were conducted in triplicate. * $p < 0.05$, ** $p < 0.01$, *** $p < 0.001$, and **** $p < 0.0001$. (data for the pure and Ag@CeO₂ systems is taken from Pugazhendhi et al. (1) and Wei et al. (2-4)).

measured for corresponding AgCNP-resistant strains (Figs. 5F



performance at 4°C (Fig. S1) reflect a retention in formulating antibacterial activity and suggest that the dominant antibacterial processes are not appreciably rate-controlled or limited by thermal activation, including metabolic processes. Follow-on studies which further probe the observed resistance are underway, though results from the current study note a more complex phase distribution of formulation components (Fig. 1) which may modify surface interactions between bacteria surface structures and the Ag/Zn-CNPs and density functional theory (DFT) studies suggest a more favorable generation of ROS relative to AgCNPs.

In the presented DFT investigation (Fig. 6, Table S1), we studied hydrogen peroxide (H_2O_2) and its dissociated products ($H/OO/H$, H/OOH , HO/OH) adsorbed on the {111}, {110} and {100} surfaces of cerium dioxide at different surface compositions including stoichiometric pure, $Ag@CeO_2$, $Zn@CeO_2$ and $Zn/Ag@CeO_2$, and oxygen deficient pure, $Ag@CeO_{2-x(SL)}$, $Zn@CeO_{2-x(SL)}$ and $Zn/Ag@CeO_{2-x(SL)}$ where the oxygen vacancy is positioned in the top layer, and oxygen deficient pure, $Ag@CeO_{2-x(SL)}$, $Zn@CeO_{2-x(SL)}$ and $Zn/Ag@CeO_{2-x(SL)}$ where the oxygen vacancy is positioned in the subsurface layer (data for the pure and $Ag@CeO_2$ systems is taken from Pugazhendhi et al. (1) and Wei et al (2)). Collectively, the computational results suggest that Ag/Zn-CNPs are more efficient in their generation of antimicrobial ROS and, therefore, potentially better able to induce virus/bacteria inactivation by an ROS-mediated pathway, relative to AgCNP or CNP alone. Results of the produced calculations, specifically, identify a less

can be interpreted as a greater ease in ROS becoming exchanged with the surrounding environment.

Considering all the models studied for all the three surfaces and the three compositions, in 55% and 69% of the models, the adsorption of ROS on $Ag/Zn@CeO_2$ is less favorable than on $Ag@CeO_2$ and CeO_2 , respectively (Fig. S3, Table S2). Considering these relationships with respect to specific surface morphologies: (1) In 60%, 50% and 57% of the {111}, {110} and {100} models, respectively, the adsorption of ROS on $Ag/Zn@CeO_2$ is less favorable than on $Ag@CeO_2$ and (2) in 60%, 67% and 86% of the {111}, {110} and {100} models, respectively, the adsorption of ROS on $Ag/Zn@CeO_2$ is less favorable than on CeO_2 . Alternatively, the data may be considered with respect to surface composition. From this representation, we find that (1) in 50%, 70% and 44% of the CeO_2 , $CeO_{2-x(SL)}$, $CeO_{2-x(SL)}$ models, respectively, the adsorption of ROS on Ag/Zn surfaces is less favorable than on the Ag surfaces alone and (2) in 50%, 90% and 67% of the CeO_2 , $CeO_{2-x(SL)}$, $CeO_{2-x(SL)}$ models, respectively, the adsorption of ROS on Ag/Zn surfaces is less favorable than on the pure surfaces alone. These results display that the presence of surface oxygen vacancies (in the $CeO_{2-x(SL)}$ models) drive the inefficiency of the Ag/Zn models compared to Ag and pure (without Ag) models.

Interestingly, despite the pronounced antimicrobial activity and favorable generation of ROS, exposure of a macrophage cell line to Ag/Zn-CNPs (Fig.S2) evidenced a non-toxic character at low concentrations: further supporting their potential use as broad-spectrum antimicrobial agents. While the current study was

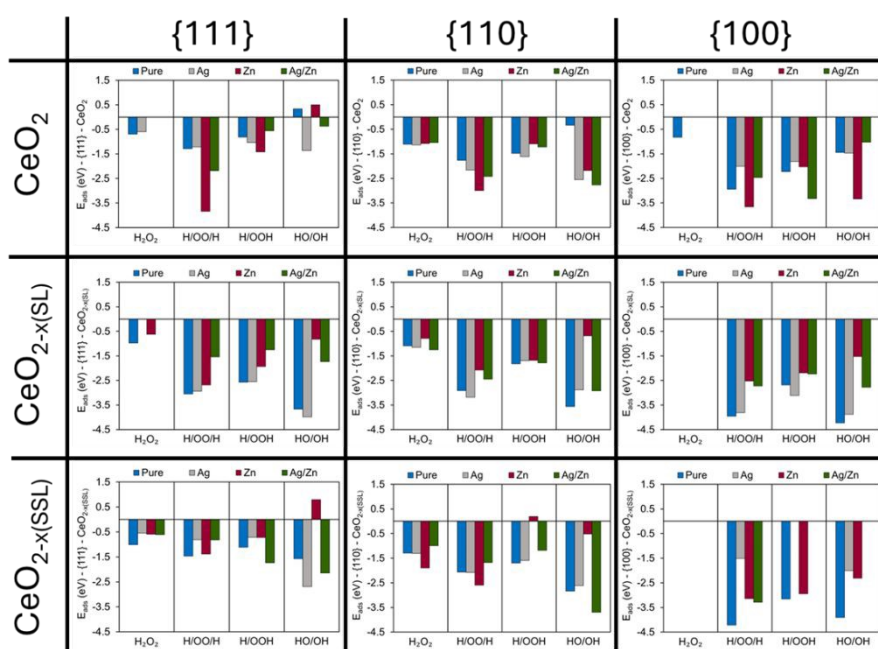


Figure 6. Density Functional Theory Schematic representation of the adsorption energies (eV). Density functional theory calculations of hydrogen peroxide (H_2O_2) and its dissociated forms ($H/OO/H$, H/OOH , HO/OH) adsorbed on the {111}, {110} and {100} surfaces of cerium dioxide at different surface compositions including stoichiometric pure, $Ag@CeO_2$, $Zn@CeO_2$ and $Zn/Ag@CeO_2$, and oxygen deficient pure, $Ag@CeO_{2-x(SL)}$, $Zn@CeO_{2-x(SL)}$ and $Zn/Ag@CeO_{2-x(SL)}$ where the oxygen vacancy is positioned in the top layer, and oxygen deficient pure, $Ag@CeO_{2-x(SL)}$, $Zn@CeO_{2-x(SL)}$ and $Zn/Ag@CeO_{2-x(SL)}$ where the oxygen vacancy is positioned in the subsurface layer. Tabulated data can be found in Table S1.

negative interaction energy for ROS with Ag/Zn-CNPs; hence, the radicals kill virus/bacteria more effectively. This relationship

designed to evaluate efficacy in disinfection, calculation of therapeutic index (TI) values from bacterial studies mark a first step in assessing material efficacy as a nano-pharmaceutical



(Fig. S4). Initial measurements in absence of biomolecules identified TI values of 2.87, 1.91, and 1.91 for *P. aeruginosa*, *S. aureus*, and MRSA, respectively. Similarly, TI values for RV14 and VSV were calculated as approximately 0.574 and 0.077, respectively. The data suggest a potential need for nanoparticle surface modification or engineering before use as a pharmaceutical. Follow-on studies of nanomaterial suitability and design for pharmaceutical applications will consider the antimicrobial efficacy of similar formulations in biological systems, with biological data and metrics such as TI, utilized for the design and optimization of nanomaterial formulations.

4. Conclusions

In the presented study, a multi-metal oxide nanoparticle formulation was produced containing zinc and silver-rich surface phases on cerium oxide nanoparticles (Ag/Zn-CNPs). Materials characterization and analyses noted a high relative proportion of cerium sites in a Ce³⁺ formal redox state, predominant metallic state for silver, and presence of zinc in both cationic Zn²⁺ and metallic Zn⁰ states, as evident from XPS measurements. High-resolution transmission electron microscopy imaging and energy-dispersive spectroscopy evidence a complex phase distribution, with elemental mapping and fast Fourier transform crystal pattern analyses suggesting presence of CeO₂, Ag⁰, and potentially (Ag,Zn)₂ phases. Treatment of bacterial (*P. aeruginosa*, *S. aureus*, MRSA) and virus (RV14 rhinovirus, VSV) species demonstrated a significant antimicrobial activity relative to a previously reported silver-modified cerium oxide nanoparticle formulation (AgCNP). Further, Ag/Zn-CNPs were found to retain antimicrobial activity towards *P. aeruginosa*, *S. aureus* strains, and RV14 lab strains which are insensitive to AgCNP treatment: further suggesting their improved utility for broad-spectrum antimicrobial technologies. Density functional theory calculations (considering presence/absence of Ce³⁺-associated oxygen vacancies, assorted high atomic density surface facets) similarly suggest a greater ability to generate antimicrobial reactive oxygen species, relative to pure pristine or non-stoichiometric cerium oxide or silver-modified cerium oxide surfaces. When the antibacterial efficacy of Ag/Zn-CNP was compared with our previously published AgCNP activity (5), data show that in the absence of biomolecules, the MIC of Ag/Zn-CNP delivered superior activity towards Gram negative *P. aeruginosa* (4 µg/mL), as well as to Gram positive *S. aureus* and MRSA (both 6 µg/mL) when compared with AgCNPs (20 µg/mL (*P. aeruginosa*) and 50 µg/mL (*S. aureus* and MRSA, unpublished data)). Notably, and in the presence of media containing biomolecules (i.e., biofouling), the MIC of Ag/Zn-CNP was found to be lower and thus more potent (30 µg/mL) when compared to AgCNPs (100 µg/mL). However, Ag/Zn-CNPs were marginally less potent to *S. aureus* and MRSA (400 µg/mL) when compared to AgCNPs (300 µg/mL). Nevertheless, and critically, the present study reveals that Ag/Zn-CNPs effectively eradicated Ag-resistant *P. aeruginosa* and *S. aureus* strains. Further, and given that bacterial antimicrobial resistance is considered a severe and global public health crisis, data confirms that remarkably,

resistant strains of *P. aeruginosa* and *S. aureus* could not be created after eight sequential sub-lethal exposure and re-culture cycles to Ag/Zn-CNP

Author contributions

Craig J. Neal: conceptualization, data curation, formal analysis, investigation, methodology, project administration, writing-original draft

Abinaya Sindu Pugazhendhi- formal analysis, investigation, methodology, data curation, writing- original draft

Elisabeth M. Shiffer- formal analysis, investigation, methodology, data curation, writing- original draft

Candace R. Fox- formal analysis, investigation, methodology, data curation, writing- original draft

Muhammad Hassan Mehmood Kalyar- formal analysis, investigation, methodology, data curation, writing- original draft

Elayaraja Kolanthai- formal analysis, investigation, methodology, data curation, writing- original draft

Katarzyna Stan-Glowinska- formal analysis, investigation, methodology, data curation, writing- original draft

Daniel Brown

Khao Minh Ta

Joanna Wojewoda-Budka

Natalia Sobczak

Marco Molinari

Griffith D. Parks- methodology, resources, supervision, writing-review & editing

Melanie J. Coathup- methodology, resources, supervision, writing- review & editing

Sudipta Seal- conceptualization, supervision, resources, writing-review & editing

Conflicts of interest

There are no conflicts of interest to declare

Data availability

The datasets supporting the findings of this study are available within the article and its supplementary information files.

Acknowledgements

Some of the TEM examination of nanoparticles was financially supported by the *Institute of Metallurgy and Materials Science* of the *Polish Academy of Sciences* within the statutory work "Modern copper composite coatings with cerium oxide particles" Z-5/2025 and the MOU between the *University of Central Florida Board of Trustees* and *Institute of Metallurgy and Materials Science Polish Academy of Sciences*. MM acknowledges the Vice Chancellor's Scholarship Scheme for funding KMT. Calculations were run on the Orion computing facility and the HPC Violeta at the University of Huddersfield, and the ARCHER2 UK National Supercomputing Services via our



membership of the UK HEC Materials Chemistry Consortium (MCC; EPSRC EP/X035859/1). SS acknowledges a NSF MRI XPS ECCS: 1726636 grant allowing XPS measurements at the UCF Materials Characterization Facility.

References

- Pugazhendhi AS, Neal CJ, Ta KM, Molinari M, Kumar U, Wei F, et al. A neoteric antibacterial ceria-silver nanozyme for abiotic surfaces. *Biomaterials*. 2024;307:122527.
- Wei F, Neal CJ, Sakthivel TS, Fu Y, Omer M, Adhikary A, et al. A novel approach for the prevention of ionizing radiation-induced bone loss using a designer multifunctional cerium oxide nanozyme. *Bioactive materials*. 2023;21:547-65.
- Wigginton KR, Kohn T. Virus disinfection mechanisms: the role of virus composition, structure, and function. *Current opinion in virology*. 2012;2(1):84-9.
- Van Dijk HF, Verbrugh HA. Resisting disinfectants. *Communications medicine*. 2022;2(1):6.
- Tong C, Hu H, Chen G, Li Z, Li A, Zhang J. Disinfectant resistance in bacteria: Mechanisms, spread, and resolution strategies. *Environmental research*. 2021;195:110897.
- Kolanthai E, Neal CJ, Kumar U, Fu Y, Seal S. Antiviral nanopharmaceuticals: Engineered surface interactions and virus-selective activity. *Wiley Interdisciplinary Reviews: Nanomedicine and Nanobiotechnology*. 2022;14(5):e1823.
- Le Ouay B, Stellacci F. Antibacterial activity of silver nanoparticles: A surface science insight. *Nano today*. 2015;10(3):339-54.
- Weiss C, Carriere M, Fusco L, Capua I, Regla-Nava JA, Pasquali M, et al. Toward nanotechnology-enabled approaches against the COVID-19 pandemic. *ACS nano*. 2020;14(6):6383-406.
- Zelikin AN, Stellacci F. Broad-spectrum antiviral agents based on multivalent inhibitors of viral infectivity. *Advanced Healthcare Materials*. 2021;10(6):2001433.
- Ivask A, ElBadawy A, Kaweeteerawat C, Boren D, Fischer H, Ji Z, et al. Toxicity mechanisms in *Escherichia coli* vary for silver nanoparticles and differ from ionic silver. *ACS nano*. 2014;8(1):374-86.
- Vasiliev G, Kubo A-L, Vija H, Kahru A, Bondar D, Karpichev Y, et al. Synergistic antibacterial effect of copper and silver nanoparticles and their mechanism of action. *Scientific Reports*. 2023;13(1):9202.
- Cagno V, Andreozzi P, D'Alicarnasso M, Jacob Silva P, Mueller M, Galloux M, et al. Broad-spectrum non-toxic antiviral nanoparticles with a virucidal inhibition mechanism. *Nature materials*. 2018;17(2):195-203.
- Punz B, Christ C, Waldl A, Li S, Liu Y, Johnson L, et al. Nano-scaled advanced materials for antimicrobial applications—mechanistic insight, functional performance measures, and potential towards sustainability and circularity. *Environmental Science: Nano*. 2025;12(3):1710-39.
- Lozovski V, Lysenko V, Piatnytsia V, Scherbakov O, Zholobak N, Spivak M. Physical point of view for antiviral effect caused by the interaction between the viruses and nanoparticles. *J Bionanosci*. 2012;6(2):109-12.
- Zholobak NM, Ivanov VK, Shcherbakov AB. Interaction of nanoceria with microorganisms. *Nanobiomaterials in antimicrobial therapy*; Elsevier; 2016. p. 419-50.
- Babenko L, Zholobak N, Shcherbakov A, Voychuk S, Lazarenko L, Spivak MY. Antibacterial activity of cerium colloids against opportunistic microorganisms in vitro. *Мікробіологічний журнал*. 2012(74, № 3):54-62. DOI: 10.1039/D5NR05105C
- Zholobak N, Olevinskaia Z, Shcherbakov A, Ivanov V, Usatenko A. Antiviral effect of cerium dioxide nanoparticles stabilized by low-molecular polyacrylic acid. *Mikrobiolohichni Zhurnal (Kiev, Ukraine: 1993)*. 2010;72(3):42-7.
- Zholobak N, Shcherbakov A, Ivanov V, Olevinskaya Z, Spivak N. Antiviral effectivity of ceria colloid solutions. *Antiviral Research*. 2011;90(2):A67.
- Nefedova A, Rausalu K, Zusinaite E, Vanetsev A, Rosenberg M, Koppel K, et al. Antiviral efficacy of cerium oxide nanoparticles. *Scientific Reports*. 2022;12(1):18746.
- Heckert EG, Karakoti AS, Seal S, Self WT. The role of cerium redox state in the SOD mimetic activity of nanoceria. *Biomaterials*. 2008;29(18):2705-9.
- Baldirim V, Bedioui F, Mignet N, Margail I, Berret J-F. The enzyme-like catalytic activity of cerium oxide nanoparticles and its dependency on Ce 3+ surface area concentration. *Nanoscale*. 2018;10(15):6971-80.
- Pirmohamed T, Dowding JM, Singh S, Wasserman B, Heckert E, Karakoti AS, et al. Nanoceria exhibit redox state-dependent catalase mimetic activity. *Chemical communications*. 2010;46(16):2736-8.
- Seal S, Jeyaranjan A, Neal CJ, Kumar U, Sakthivel TS, Sayle DC. Engineered defects in cerium oxides: tuning chemical reactivity for biomedical, environmental, & energy applications. *Nanoscale*. 2020;12(13):6879-99.
- Verma A, Stellacci F. Effect of surface properties on nanoparticle-cell interactions. *small*. 2010;6(1):12-21.
- Keshavan S, Calligari P, Stella L, Fusco L, Delogu LG, Fadeel B. Nano-bio interactions: a neutrophil-centric view. *Cell Death & Disease*. 2019;10(8):569.
- Agarwal S, Lefferts L, Mojet BL. Ceria nanocatalysts: shape dependent reactivity and formation of OH. *ChemCatChem*. 2013;5(2):479-89.
- Aneggi E, Llorca J, de Leitenburg C, Dolcetti G, Trovarelli A. Soot combustion over silver-supported catalysts. *Applied Catalysis B: Environmental*. 2009;91(1-2):489-98.
- Kayama T, Yamazaki K, Shinjoh H. Nanostructured ceria-silver synthesized in a one-pot redox reaction catalyzes carbon oxidation. *Journal of the American Chemical Society*. 2010;132(38):13154-5.
- Preda G, Pacchioni G. Formation of oxygen active species in Ag-modified CeO2 catalyst for soot oxidation: A DFT study. *Catalysis today*. 2011;177(1):31-8.
- Mitsudome T, Mikami Y, Matoba M, Mizugaki T, Jitsukawa K, Kaneda K. Design of a silver-cerium dioxide core-shell nanocomposite catalyst for chemoselective reduction reactions. *Angewandte Chemie International Edition*. 2012;51(1):136-9.
- Al-Haddad J, Alzaabi F, Pal P, Rambabu K, Banat F. Green synthesis of bimetallic copper-silver nanoparticles and their application in catalytic and antibacterial activities. *Clean Technologies and Environmental Policy*. 2020;22(1):269-77.
- Formaggio DMD, de Oliveira Neto XA, Rodrigues LDA, de Andrade VM, Nunes BC, Lopes-Ferreira M, et al. In vivo toxicity and antimicrobial activity of AuPt bimetallic nanoparticles. *Journal of Nanoparticle Research*. 2019;21(11):244.
- Merugu R, Gothalwal R, Deshpande PK, De Mandal S, Padala G, Chitturi KL. Synthesis of Ag/Cu and Cu/Zn bimetallic nanoparticles using toddy palm: Investigations of their antitumor, antioxidant and antibacterial activities. *Materials Today: Proceedings*. 2021;44:99-105.
- Andrade GR, Nascimento CC, Lima ZM, Teixeira-Neto E, Costa LP, Gimenez IF. Star-shaped ZnO/Ag hybrid nanostructures for enhanced



- photocatalysis and antibacterial activity. *Applied Surface Science*. 2017;399:573-82.
35. Fox CR, Kedarinath K, Neal CJ, Sheiber J, Kolanthai E, Kumar U, et al. Broad-spectrum, potent, and durable ceria nanoparticles inactivate RNA virus infectivity by targeting virion surfaces and disrupting virus–receptor interactions. *Molecules*. 2023;28(13):5190.
36. Neal CJ, Fox CR, Sakthivel TS, Kumar U, Fu Y, Drake C, et al. Metal-mediated nanoscale cerium oxide inactivates human coronavirus and rhinovirus by surface disruption. *ACS nano*. 2021;15(9):14544-56.
37. Kresse G, Furthmüller J. Efficient iterative schemes for ab initio total-energy calculations using a plane-wave basis set. *Physical review B*. 1996;54(16):11169.
38. Kresse G, Hafner J. Ab initio molecular-dynamics simulation of the liquid-metal–amorphous-semiconductor transition in germanium. *Physical Review B*. 1994;49(20):14251.
39. Kresse G, Joubert D. From ultrasoft pseudopotentials to the projector augmented-wave method. *Physical review b*. 1999;59(3):1758.
40. Blöchl PE. Projector augmented-wave method. *Physical review B*. 1994;50(24):17953.
41. Perdew JP, Burke K, Ernzerhof M. Generalized gradient approximation made simple. *Physical review letters*. 1996;77(18):3865.
42. Ta KM, Neal CJ, Coathup M, Seal S, Gillie LJ, Cooke DJ, et al. The Buffering Activity of Ceria toward Reactive Oxygen Species: A Density Functional Theory Perspective. *The Journal of Physical Chemistry C*. 2025.
43. Dudarev SL, Botton GA, Savrasov SY, Humphreys C, Sutton AP. Electron-energy-loss spectra and the structural stability of nickel oxide: An LSDA+ U study. *Physical Review B*. 1998;57(3):1505.
44. Molinari M, Parker SC, Sayle DC, Islam MS. Water adsorption and its effect on the stability of low index stoichiometric and reduced surfaces of ceria. *The Journal of Physical Chemistry C*. 2012;116(12):7073-82.
45. Munir S, Smith T, Ta KM, Gillie LJ, Cooke DJ, Molinari M. Modelling hydrogen peroxide adsorption on cerium dioxide: the effect of surface strain. *Catalysis Science & Technology*. 2025;15(17):5150-66.
46. Munir S, Ta KM, Smith T, Gillie LJ, Cooke DJ, Parker SC, et al. Strain Effects on the Adsorption of Water on Cerium Dioxide Surfaces and Nanoparticles: A Modeling Outlook. *The Journal of Physical Chemistry C*. 2024;128(43):18451-64.
47. TobyáKelsey E, áde Leeuw NH. Atomistic simulation of dislocations, surfaces and interfaces in MgO. *Journal of the Chemical Society, Faraday Transactions*. 1996;92(3):433-8.
48. Brambila C, Sayle D, Molinari M, Nutter J, Flitcroft J, Sayle T, et al. Tomographic study of mesopore formation in ceria nanorods. *The Journal of Physical Chemistry C*. 2021;125(18):10077-89.
49. Molinari M, Symington AR, Sayle DC, Sakthivel TS, Seal S, Parker SC. Computer-aided design of nanoceria structures as enzyme mimetic agents: The role of bodily electrolytes on maximizing their activity. *ACS Applied Bio Materials*. 2019;2(3):1098-106.
50. Moxon S, Symington AR, Joshua ST, Flitcroft JM, Skelton JM, Gillie LJ, et al. Composition-dependent morphologies of CeO₂ nanoparticles in the presence of Co-adsorbed H₂O and CO₂: a density functional theory study. *Nanoscale*. 2024;16(23):11232-49.
51. Symington AR, Harker RM, Storr MT, Molinari M, Parker SC. Thermodynamic evolution of cerium oxide nanoparticle morphology using carbon dioxide. *The Journal of Physical Chemistry C*. 2020;124(42):23210-20.
52. Symington AR, Molinari M, Moxon S, Flitcroft JM, Sayle DC, Parker SC. Strongly bound surface water affects the shape evolution of cerium oxide nanoparticles. *The Journal of Physical Chemistry C*. 2020;124(6):3577-88.
53. Ta KM, Cooke DJ, Gillie LJ, Parker SC, Seal S, Wilson PB, et al. Infrared and Raman diagnostic modeling of phosphate adsorption on ceria nanoparticles. *The Journal of Physical Chemistry C*. 2023;127(40):20183-93.
54. Ta KM, Wisdom DO, Gillie LJ, Cooke DJ, Zhu R, Gonçalves MA, et al. Sorption of arsenate on cerium oxide: a simulated infrared and Raman spectroscopic identification. *Environmental Science: Nano*. 2025;12(3):1896-907.
55. Hierholzer J, Killington R. Virus isolation and quantitation. *Virology methods manual*: Elsevier; 1996. p. 25-46.
56. Long Z, Kang L, Yin F, Li Z, Zhao M, Liu Y, et al. Phase equilibria of the Ag–Zn–Ce (0–33.3 at.% Ce) system at 450° C and 600° C. *Journal of alloys and compounds*. 2015;618:172-81.
57. Gschneidner K, Calderwood F. The Ag-Ce (Silver-Cerium) system. *Bulletin of Alloy Phase Diagrams*. 1985;6(5):439-43.
58. Chiotti P, Mason J. Phase relations and thermodynamic properties for the cerium-zinc systems. *Trans Met Soc AIME*. 1965;233.
59. Gomez-Acebo T. Thermodynamic assessment of the Ag-Zn system. *Calphad*. 1998;22(2):203-20.
60. Kourouklis G, Jayaraman A, Espinosa G. High-pressure Raman study of CeO₂ to 35 GPa and pressure-induced phase transformation from the fluorite structure. *Physical Review B*. 1988;37(8):4250.
61. Kuchibhatla SV, Karakoti AS, Baer DR, Samudrala S, Engelhard MH, Amonette JE, et al. Influence of aging and environment on nanoparticle chemistry: implication to confinement effects in nanoceria. *The Journal of Physical Chemistry C*. 2012;116(26):14108-14.
62. Korsvik C, Patil S, Seal S, Self WT. Superoxide dismutase mimetic properties exhibited by vacancy engineered ceria nanoparticles. *Chemical communications*. 2007(10):1056-8.
63. Neal CJ, Sakthivel TS, Fu Y, Seal S. Aging of nanoscale cerium oxide in a peroxide environment: Its influence on the redox, surface, and dispersion character. *The Journal of Physical Chemistry C*. 2021;125(49):27323-34.





UNIVERSITY OF CENTRAL FLORIDA

**Materials Science & Eng (MSE), AMPAC, Nanoscience Technology Center, College of
Medicine**

Room 207, Eng.1, Orlando, FL, 32816

December 1, 2025

To
The Editor,
Nanoscale

Data Availability Statement

The datasets supporting the findings of this study are available within the article and its supplementary information files.

We hope that you find the manuscript suitable for publication in *Nanoscale*.

Sincerely

A handwritten signature in black ink, appearing to read 'Sudipta Seal', written over a horizontal line.

Sudipta Seal, Ph.D.

Trustee Chair, University Distinguished Professor and Pegasus Professor, Chair: MSE

